Chapter 21
Interactions Between Molten Iron and Carbon Bonded Filter Materials

Xingwen Wei, Enrico Storti, Steffen Dudczig, Olga Fabrichnaya, Christos G. Aneziris, and Olena Volkova

21.1 Introduction

The detrimental effects of the non-metallic inclusion strongly impair the mechanical properties of the final products [1, 2]. In particular, the macro inclusion or the inclusions clusters could lead to the cracks in the final metallic products. Therefore, to improve the cleanness of the metallic products and meet the new market's requirement, it is urgent to minimize the amount of the inclusions in the melts. Ceramic foam filters are considered as a one of the most efficient methods to extract inclusions from the molten liquids though the deposition of inclusions on the ceramic surface. Besides the good attractive nature for the inclusions, the ceramic foam materials should also overcome the great temperature difference in and out of the molten liquids, i.e. the thermal shock resistance.

The addition of carbon could contribute to the improvement of thermal shock resistance of ceramics. Afterward, carbon bonded ceramics filters such as foam (Al_2O_3-C) filters with Al_2O_3 and with carbon bonded MgO coatings for the steel melt filtration were developed [3–5]. Further, to test the filtration efficiency, these filters were immersed into 42CrMo4 steel melts at 1650 °C. Alumina and magnesia layers were detected at the surface of Al_2O_3-C filter and of the Al_2O_3-C filter coated with carbon

X. Wei (✉) · O. Volkova
Institute of Iron and Steel Technology, Technische Universität Bergakademie Freiberg, Leipziger Str. 34, 09599 Freiberg, Germany
e-mail: Xingwen.wei@iest.tu-freiberg.de

E. Storti · S. Dudczig · C. G. Aneziris
Institute of Ceramics, Refractories and Composite Materials, Technische Universität Bergakademie Freiberg, Agricolastraße 17, 09599 Freiberg, Germany

O. Fabrichnaya
Institute of Material Science, Technische Universität Bergakademie Freiberg, Gustav-Zeuner-Str. 5, 09599 Freiberg, Germany

bonded MgO. Furthermore, a massive of Al_2O_3 and MgO inclusions were found to accumulate onto the newly formed layers. In contrary, the alumina coated surface remained clean and without the deposition of inclusions [6]. Moreover, the study of [6, 7] also stated the detection of oxides whisker after the carbon bonded ceramic filters materials making the contact with the melts. The composition of whiskers was related to the constitution of the interacted filters materials. The mechanism of the newly formed layers was studied by immersing the carbon bonded filters into the liquids (finger test) [8–10] and interacting with liquid alloy [11]. The formation of the whiskers was investigated in the work of [12]. Besides the above-mentioned carbon boned substrates, calcium aluminates CA2 and CA6 were coated onto the Al_2O_3-C filter and further immersed into the melts for 10 s [13]. After the immersion test, a secondary oxide layer with fine inclusions were observed on filters. Both types of filters delivered satisfying filtration efficiency for non-metallic inclusions.

Based on the literature survey, the presence of carbon was believed to be the reason for the formation of new layers on the filters. The released aluminum for the later formation of the secondary alumina layer was believed to be contributed by the carbothermic reduction of alumina with the presence together of steel and carbon [14]. However, the dissolution mechanism of alumina into melts was later stated in the work of [15] and supported by the calculated simulation. The unclear mechanism that related to the alumina 'reduction' was completely studied by interacting four different types of carbon (10 wt% C) bonded ceramics C-Al_2O_3, Al_2O_3 rich spinel (C-AR78), MgO rich spinel (C-MR66), and $CaO·6Al_2O_3$ (C-CA6) with liquid Armco iron to investigated the possible reactions that induced by the presence of carbon.

In addition, the work of [16] indicated that the inclusions removal efficiency or filtration efficiency is strongly related to the wetting behavior of the inclusions. Therefore, the wettability of the pure ceramics substrates was investigated (1). Al_2O_3 based containing high MgO (MR66), (2). $MgAl_2O_4$ spinel based containing MgO (AR 78), (3). CA 6 ($CaO·6Al_2O_3$), (4). $CaZrO_3$, and (5). Al_2O_3 based containing TiO_2 and ZrO_2 (AZT). Furthermore, after the interaction, the quantity, size, and the composition of the inclusions was analyzed by utilizing an automatic scanning electron microscope combined with an energy dispersive X-Ray spectroscope (EDX) (Aspex, FEI, USA).

21.2 Experimental Procedure

21.2.1 The Preparation of the Substrates

Table 21.1 summarized the raw oxides used for the preparation of the substrates. For the pure ceramic substrates preparation, the additives were dextrin (used as binder for the granulation), Optapix AC95 and PAF35 (Zschimmer & Schwartz— used as temporary binders), Zusoplast G112. On the other hand, for carbon bonded materials carbon black was added to get 10 wt% residual carbons after coking. The

Table 21.1 Raw oxide used for the preparation of the substrates and the related parameters

Substrate material	Raw material(s)	Grain size (d90) (μm)	Roughness (μm)
C-Al$_2$O$_3$	10 wt% + Al$_2$O$_3$	<20	5.5
C-CA6 Bonite	10 wt% + CA6	<20	4.04
C-AR78 spinel	10 wt% + AR78	<20	3.70
C-MR66 spinel	10 wt% + MR66	<90	9.18
MR 66	91.5% Al$_2$O$_3$, 8.5% MgO	<90	2.15
AR 78	99.7% MgAl$_2$O$_4$, 0.3% MgO	<20	2.05
CaZrO$_3$	83.3% CaZrO$_3$, 16.7% ZrO$_2$	<45	3.37
CA 6	94.9% CA 6 (CaO·6Al$_2$O$_3$), 5.0% Al$_2$O$_3$, 0.1% CaO	<20	1.57
AZT	95% Al$_2$O$_3$, 2.5% TiO$_2$ 2.5% ZrO$_2$	<60	8.24

samples were bonded using powder novolac resin and hexametilentetramine as a curing agent. Then, the substrate samples were polished with ultra-fine SiC sandpaper (down to 3 μm particle size). The X-ray diffraction analysis (XRD) was conducted after heat treatment to determine the phase composition of the substrates before the interaction experiments. The instrument (X'Pert PRO MPD X-Ray Diffractometer 3040/60, PANalytical, Germany) operates in Bragg–Brentano geometry with a fixed divergence slit and a rotating sample stage. The parameters were standard Cu Kα radiation (λ = 1.54 Å), a 2θ-range from 7.5 to 90° with a scan step size of 0.013° and a holding time of 30 s per step. Later, the surface of the substrates confocal laser scanning microscopy (CLS) measured. An area of 5 × 5 mm^2 for each polished sample was scanned. The roughness results obtained by laser microscopy and open porosity was estimated by means of water immersion, according to the European standard DIN EN 993–1. The measured results are summarized in Table 21.1. A more in-detailed description for the preparation of substrates was reported elsewhere [12].

21.2.2 Experimental Setup

The Armco iron, with the chemical composition listed in Table 21.2, was used for the investigations in contact with pure and carbon bonded substrates. The Armco iron samples with a diameter of 7.5 mm and a mass of 2.5 g were prepared and cleaned in an ultrasound device with ethanol and then etched with HCl. The experiments were carried out inside a high temperature microscope using the sessile drop method. Before heating, the chamber of the microscope was evacuated to 10^{-4} atm for the elimination of oxygen. After evacuation, the heating program was started. Thereby, the samples were heated with a heating rate of 40 K/min under Argon atmosphere (Ar 5.0 containing 2–3 ppm oxygen) to the target temperature of 1600 °C for pure

Table 21.2 Composition of Armco iron (Trace elements in ppm)

Fe (wt%)	C	Mn	Si	Al	S	P	O
99.8	40	200	50	<10	40	64	92

ceramics and 1625 °C for carbon bonded ceramics. The Argon gas flow rate was 0.3 L/min. The samples were held at the target temperature for 30 min and 2 h for pure ceramics and carbon bonded ceramics, respectively. The droplet silhouette of molten iron was examined from the video material recorded by an Image Source CCD camera. The setup schema is shown in Fig. 21.1.

To compare with the experiments between liquid Armco iron and carbon bonded substrates, a piece of carbon bonded alumina (C-Al$_2$O$_3$) was insert into a platinum container and a quartz glass ampule to ensure a better atmosphere such as (1). Cleanness, (2). Elimination of the influence of gas flow. Furthermore, a gap and orifice were kept between platinum crucible and lid, and on a side of the ampule to ensure the identical atmosphere in crucible and chamber (as shown in Fig. 21.2), which enhanced the reliability of the experiment.

The oxygen content in the experimental atmosphere is controlled by O/CO system, the installed graphite tube for heating process acted as oxygen eliminator by formation of CO and CO$_2$ gas [17]. The oxygen partial pressure in high temperature microscope was measured during the experiments using a high temperature zirconia oxygen probe, which was installed at the gas outlet. The oxygen partial pressure was calculated according to Eq. (21.1)

$$P(o_2) = 0.2094 \times 10^{\left(\frac{-20.166}{T}\right)EMF} \tag{21.1}$$

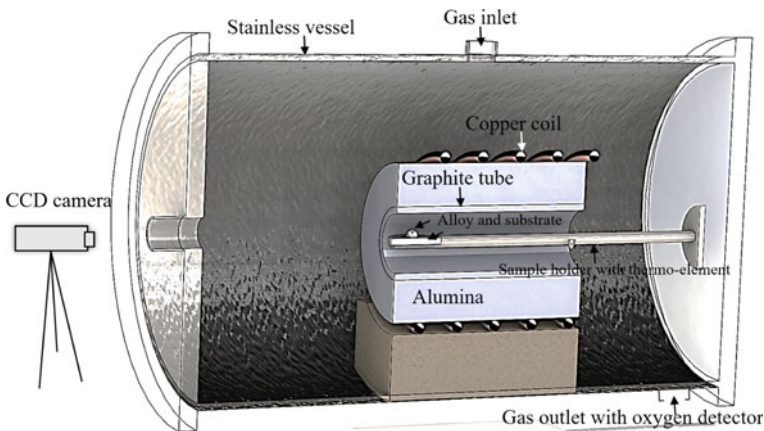where T is Temperature (K) and EMF is sensor signal (mV).

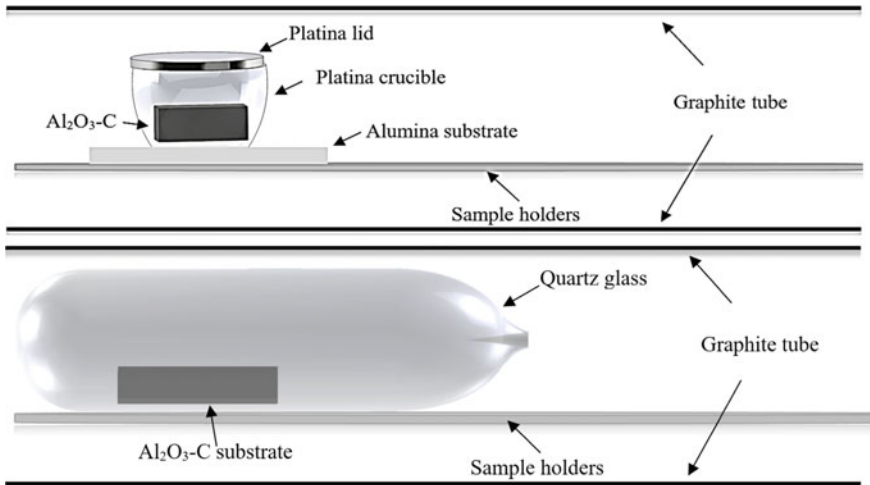**Fig. 21.1** Schematic view of setup, a cross section

Fig. 21.2 Platinum crucible [12] and quartz glass illustration

For the pure substrates, the oxygen partial pressure was kept constantly at 10^{-21} atm. In the carbon bonded substrates system, the oxygen partial pressure was lower than for the system without carbon due to the carbon oxidation. In the C-Al_2O_3 and C-CA 6 cases, the measured oxygen partial pressure is 10^{-24} atm. Furthermore, in the C-AR 78 is $P_{O2} = 10^{-25}$ atm. A lower oxygen content ($P_{O2} = 10^{-26}$ atm at 1625 °C) was detected in the C-MR 66 substrate case.

The spark spectrometer Foundry-Master UV (Oxford Instruments) was employed for the general chemical analysis of the iron samples. Besides, Bruker G4 Ikarus and Bruker G8 Galileo combustion analyzers were utilized to estimate the C, O, and S values. Scanning electron microscopy (SEM) in combination with Energy-Dispersive X-ray Spectroscopy (EDX) were used for morphology and chemical composition analyses (Ultra55, Zeiss NTS GmbH). After the experiments, for pure substrates-iron samples, the solidified iron was pressed into a plate with 1 mm thickness then measured the chemical composition. The cross sectional area between substrates and iron was analyzed by SEM/EDX. On the other hand, carbon bonded substrates and iron samples were entirely embedded in epoxy resin and perpendicularly cut for the cross section SEM/EDX analysis.

21.2.3 Non-metallic Inclusions Determination

After the interaction with pure substrates, the solidified iron droplets were embedded in epoxy resin and cut at the thickest area of the iron droplet from the bottom area and then polished. Afterwards, an automatic scanning electron microscope combined

Table 21.3 Developed Rule-file applied for Aspex-SEM inclusions classification [18]

Class name	Element content (wt%)
Al_2O_3	Al > 20 and O > 20 and Si < 10 and Ti < 10 and (Mn + Mg + Si + Ca + Ti) < 10 and Mn < 10
TiN	Ti > 10 and N > 5
MnO-Al_2O_3	Al > 10 and Mn > 2 and (Mg + Si + Ca + Ti) < 10 and Si < 2 and S < 2
MnO-SiO_2-high Al_2O_3	Mn > 2 and Si > 2 and Al > 15
MnO-SiO_2-low Al_2O_3	Mn > 2 and Si > 2 and 1 < = Al < 15
MnO-SiO_2-TiO_2	Mn > 2 and Si > 2 and Al < 1 and Ti > 2
SiO_2	Si/O > = 0.4 and Si/O < 6.2 and Al < 3 and Mg < 3 and Ca < 3 and K < 3 and Mn < 3 and S < 10
SiO_2-MnO	Si/Mn > = 0.7 & Ca < = 0
MnO-MnS	Mn > 8 and (Mn/S) > = 1 and (Al + Si + Ti + Cr) < (Mn + S)
CaO-Al_2O_3-SiO_2	Ca > 5 and Al > 5 and Si > 5
CaO-CaS	Ca > 5 and (Ca/S) > 2
Other	Fe < 100

with an energy dispersive X-Ray spectroscope (EDX) Aspex was applied to determine the non-metallic inclusions distribution and their chemical composition. A developed rule file for the inclusions classification is presented in Table 21.3. A more in-detailed description for the inclusions analysis was reported elsewhere [18].

21.3 Results and Discussion

21.3.1 Carbon Bonded Substrates

Figure 21.3 presents the Armco iron samples on the carbon bonded substrate. It can be apparently seen that, the iron samples transferred to non-symmetrical form. Expect for the MR66 case, whiskers were also observed on the surface of the iron sample. In addition, crystals were found to form on the substrate as pointed with arrow. Normally, the iron sample would form a perfect droplet due to surface tension. However, in the present case, the iron samples were covered by the newly formed phase.

Figure 21.4 presents the images of the cooled iron with the contacted carbon bonded substrates. As shown in Fig. 21.4, the carbon bonded substrates were found strongly modified after the interaction between liquid Armco iron and carbon bonded substrates.
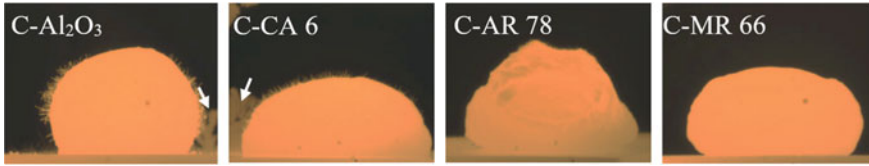
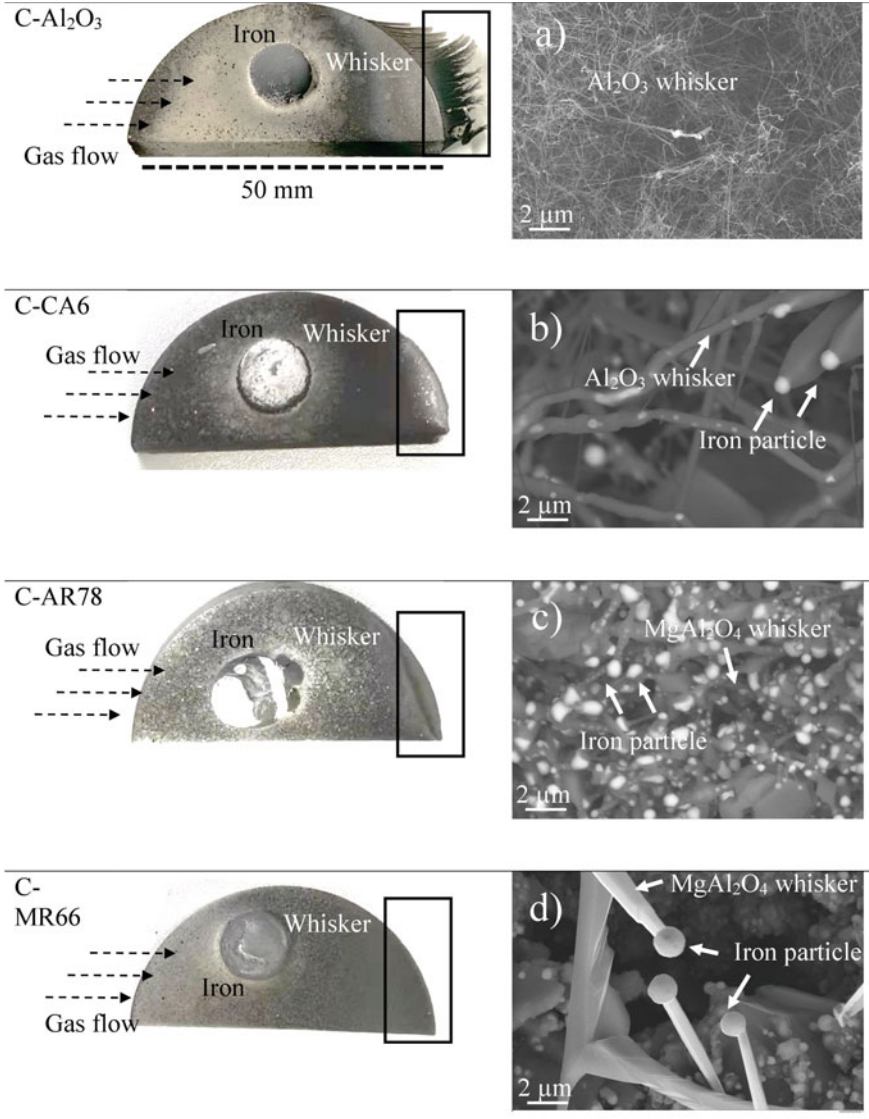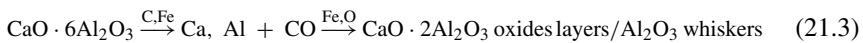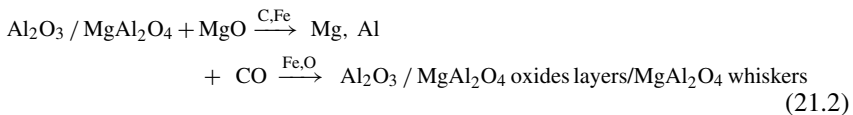**Fig. 21.3** Images of iron on carbon bonded substrates [12]

Fig. 21.4 Images of carbon-bonded substrates after interaction with molten iron and morphology of iron capped whiskers. **a** C-Al$_2$O$_3$; **b** C-CA 6; **c** C-AR 78; **d** C-MR 66 [12, 20]

(1) The interfacial color change of the substrates from black to the grey color indicate the great decarburization process. The current used Armco iron sample contains 40 ppm of carbon, this low carbon content indicates a great carbon adsorption tendency of the liquid Armco iron. Furthermore, as already mentioned in the experimental part, the introduced protective gas Argon 5.0 contains also 2–3 ppm oxygen. Therefore, the carbon on interfacial area of the substrates could also been consumed by the oxygen contained in the protective gas.

(2) The formation of oxide layers covering on the iron sample.

(3) The formation of whiskers. The newly formed whiskers were classified as two groups, i.e. with and without the iron particles capping. According to Xie et al. [19], the iron capped whiskers formed by the released elements that dissolved in the melt until its super-saturation, then the whisker starts to grow. Wei et al. [12] stated one more mechanism for the whiskers formation. Here, Wei et al. detected the solid phases Al_4C_3 and Al_4O_4C after the interaction with liquid Armco iron at 1625 °C, as well as the thermodynamic simulation. Afterwards, he stated that the newly formed Al_4C_3 and Al_4O_4C could be oxidized in CO atmosphere and contribute to the alumina whiskers formation.

In Fig. 21.5, the cross sectional analysis of iron and carbon bonded substrates is presented. The newly formed layers covered on the iron sample were revealed as Al_2O_3, $MgAl_2O_4$, $CaO \cdot 2Al_2O_3$, and $MgAl_2O_4$ for C-Al$_2$O$_3$, C-AR78, C-CA 6, and C-MR66, respectively. Moreover, iron was found to penetrate into the substrates, especially for C-Al$_2$O$_3$ and C-CA 6 substrates. For C-AR78 and C-MR66 substrates, the iron penetration was prevented by the newly formed oxide layers that covered on the iron samples. In the case of C-Al$_2$O$_3$ substrate, Al_2O_3 plates was detected accumulated on a newly formed alumina layer. In Fig. 21.5f, a macro non-metallic inclusion $MgAl_2O_4$ with SiO_2 as core in the side of iron was detected. According to the results, the newly formed oxide layers was found to cover on the iron sample and the whiskers formation are related to the composition of the substrates. In other words, it may conclude that the oxide layers consisting elements (Al, Mg, Ca, and O) were released within the interaction process. A proposed mechanism for the elements releasing and the oxides and whiskers formation is presented in Eqs. (21.2) and (21.3).
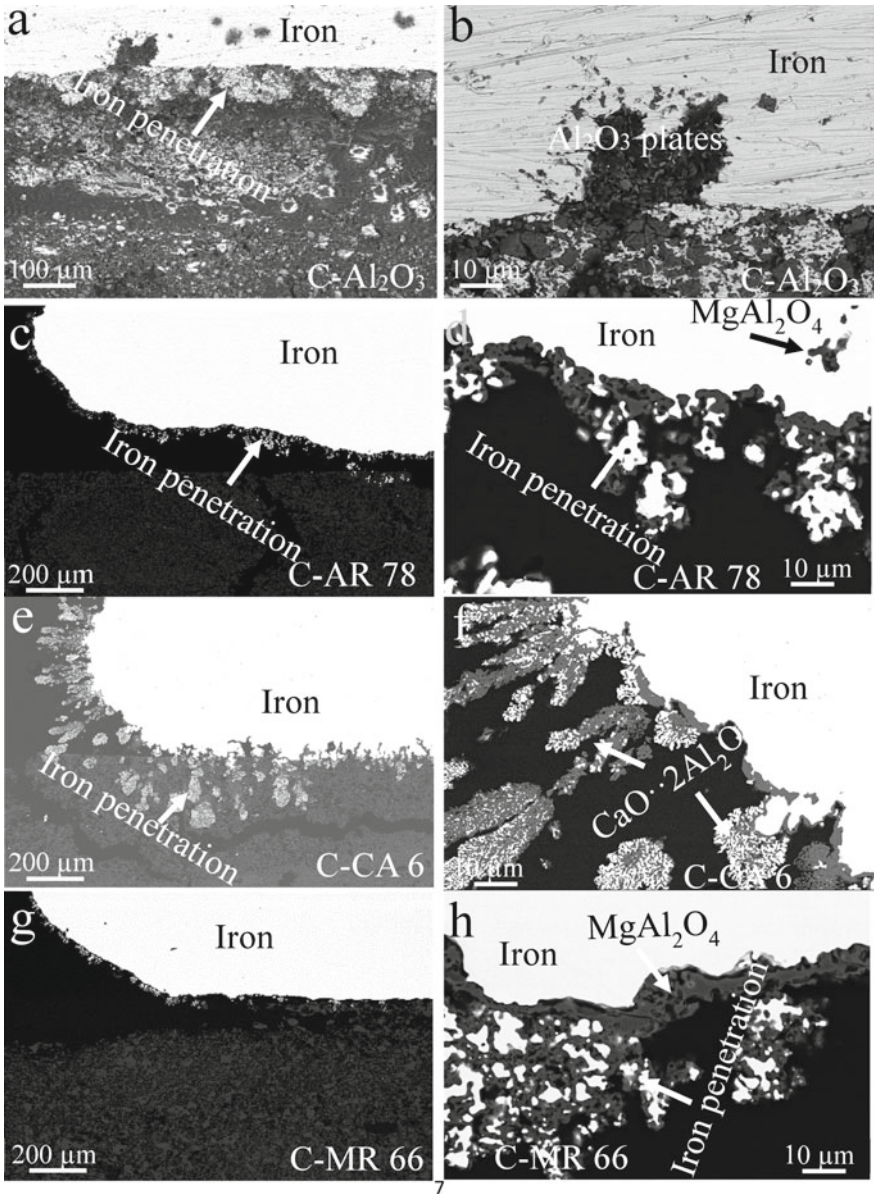
$$Al_2O_3 \text{ / } MgAl_2O_4 + MgO \xrightarrow{C,Fe} Mg, \text{ } Al$$
$$+ \text{ } CO \xrightarrow{Fe,O} \text{ } Al_2O_3 \text{ / } MgAl_2O_4 \text{ oxides layers/} MgAl_2O_4 \text{ whiskers}$$
(21.2)

$$CaO \cdot 6Al_2O_3 \xrightarrow{C,Fe} Ca, \text{ } Al \text{ } + \text{ } CO \xrightarrow{Fe,O} CaO \cdot 2Al_2O_3 \text{ oxides layers/} Al_2O_3 \text{ whiskers} \quad (21.3)$$

Fig. 21.5 Cross section of iron with the carbon bonded substrates. **a**, **b** C-Al$_2$O$_3$; **c**, **d** C-AR78; **e**, **f** C-CA 6; **g**, **h** C-MR66 [20]

Quartz Glass Ampule and Platina Crucible

The quenched quartz glass ampule was roughly smashed, the microstructure and compositions of the inner/outside surface of ampule and the graphite alumina were carefully analysed with the aid of SEM/EDX as shown in Fig. 21.6.

The idea is that, the for measured whiskers, however were determined as SiO_2 whiskers. But it contains a noticeable Al. Specially the area outside of the ampule. SiO_2 has no effects on producing Al or Al containing gas. The Al observed areas (whiskers) which are far away from the graphite alumina may indicates the reduction process of alumina. In the present case, carbon is the only substance capable for these reduction process.

The investigated experiments without the presence of iron states that the aluminium releasing may occur without the aid of the iron. The shapes of whiskers in both experiments are very different from the results in presence of iron. For the graphite alumina inserted quartz glass ampule system a schematic illustration is shown in Fig. 21.7. Based on the achieved results, the aluminium is apparently released from the C- Al_2O_3 and the most gas products of aluminium could be Al_2O, AlO, and Al, resulting in the detected whiskers crystals on the surface of graphite alumina and in the orifice area, owing to the deoxidation and precipitation reactions. In addition, AlO reacts with CO gas forms alumina as well. The detected Si is owing to the reduction process between SiO_2 and C. In fact, the formation of Si containing gas (SiO) and reoxidation reactions is very complicated. Biernacki and Wotzak [21] have created a mechanism which shown as Eqs. (21.4)–(21.6). The silicon carbide (SiC) will be formed by the reaction of silica (SiO_2) and carbon (C), then SiO_2 reacts with SiC further produce SiO gas. The produced gas SiO will further react with CO and O_2 gas to form SiO_2.

$$SiO_2 + 3C = SiO_{(g)} + 2CO_{(g)} \qquad (21.4)$$
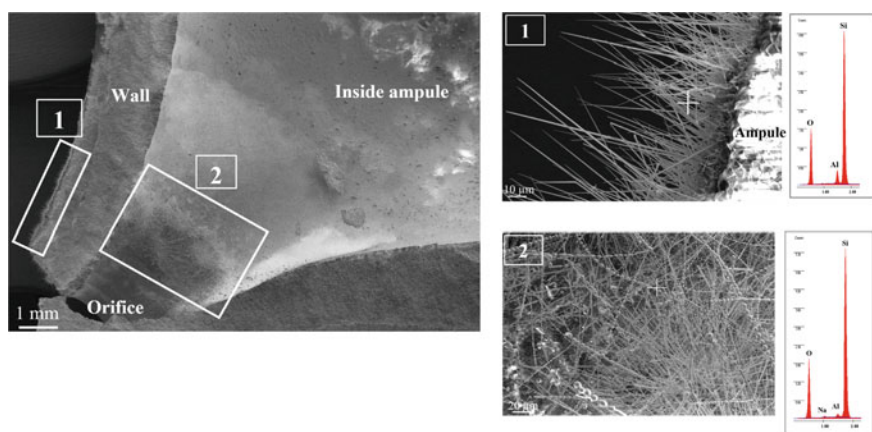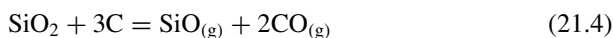

Fig. 21.6 Microstructure and EDX analyses of the quartz glass ampule system on spot 1 and 2
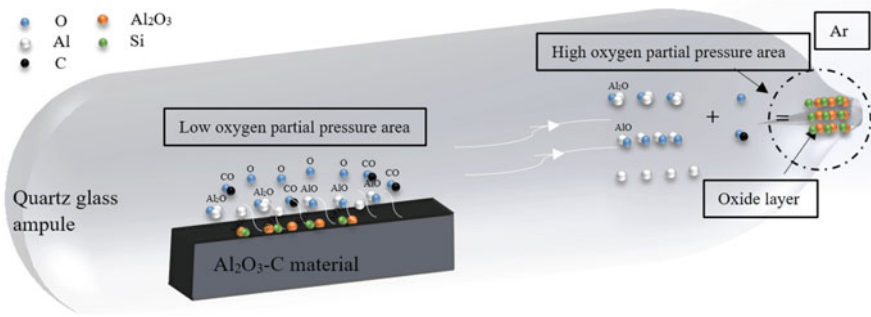
Fig. 21.7 Schematic illustration of the graphite alumina inserted quartz glass ampule system

$$SiO_{2(g)} + 2C = SiC + CO_{(g)} \tag{21.5}$$

$$SiC + 2SiO_2 = 3SiO + CO_{(g)} \tag{21.6}$$

$$SiO + O = SiO_2 \tag{21.7}$$

$$SiO + CO = SiO_2 \tag{21.8}$$
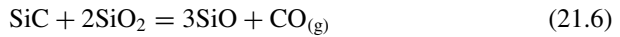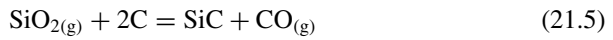
The produced gas products increase the local pressure in ampule system, it led to the released gas products tend to leave the ampule to balance the entire system. On the other side, the raised pressure in ampule blocked the entrance for oxygen as well. Therefore, a significant oxide layer formed on the orifice area. Finally, although the Si can react with alumina, but the detected aluminium located far away from the graphite material which is considered as released with the help of carbon.

In Fig. 21.8 presented the image of the heated carbon bonded alumina in platina crucible. Whiskers on the surface carbon bonded alumina was determined. Figure 21.9 presented the morphology structure of the detected whiskers and its XRD analysed results. The achieved XRD result on the detected dendritic whiskers is presented in Fig. 21.9b, it consisted of alumina.

Based on the detected alumina whiskers on the carbon bonded material, it can be concluded that iron may not have a decisive effect on the carbothermic reduction, since the aluminium release process occurs without the presence of iron. But, on the other hand, the catalytic effect of iron cannot be denied. With the presence of iron, the aluminium releasing process could possibly be enhanced. The explanation for the metallic elements releasing such as Al, Ca, Mg is shown in the later sections with the support of stability of various oxides that existed in present study.
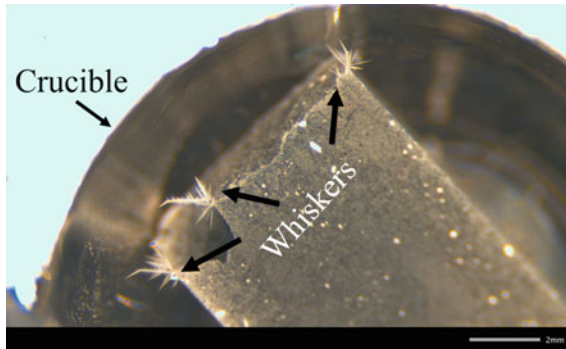
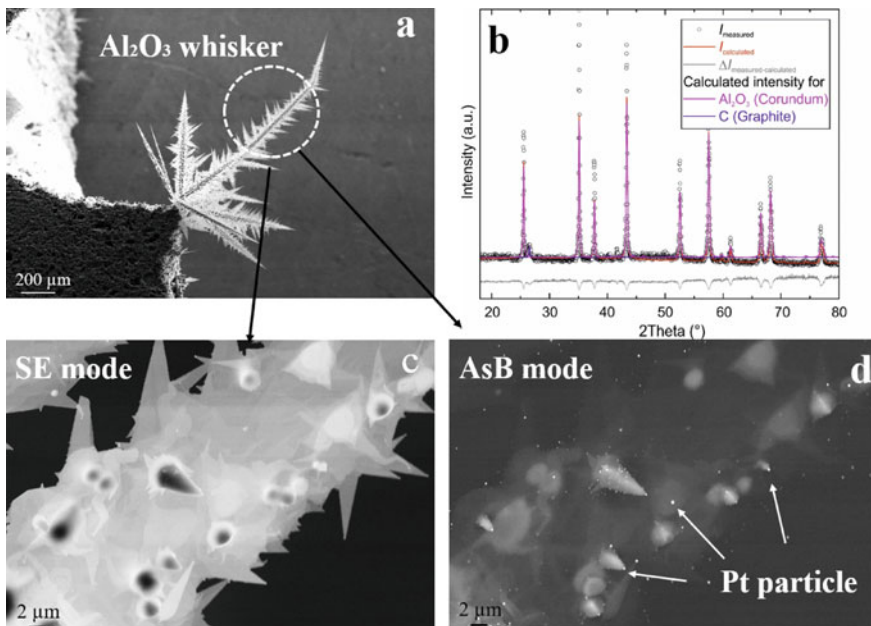Fig. 21.8 Image of the carbon bonded alumina in platina crucible after heating

Fig. 21.9 Morphology of the alumina whiskers on the surface of Al_2O_3-C material (**a**, **c** and **d**). **b** XRD profile of dendritic whiskers [12]

21.3.2 Pure Substrates

The measured contact angle on various substrates were presented in Fig. 21.10. Besides the AZT substrate, the contact angles of all cases exhibited slightly varied value. The contact angle on the AZT substrate increased slightly from the initial time point from 127.3° to 128.4° at 10 min and then decreased to 126.7° at 30 min. Such
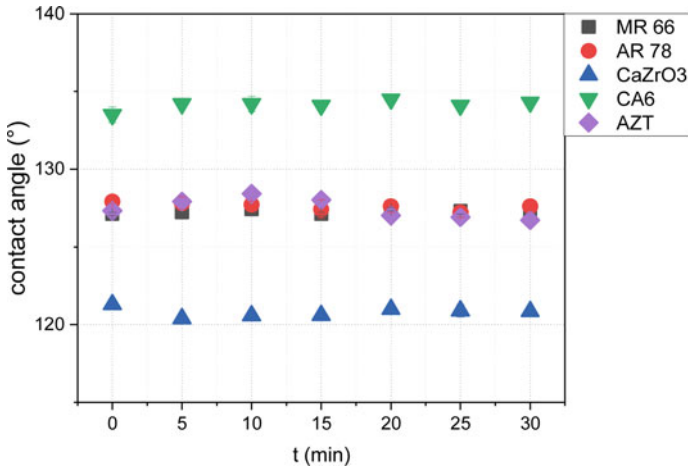
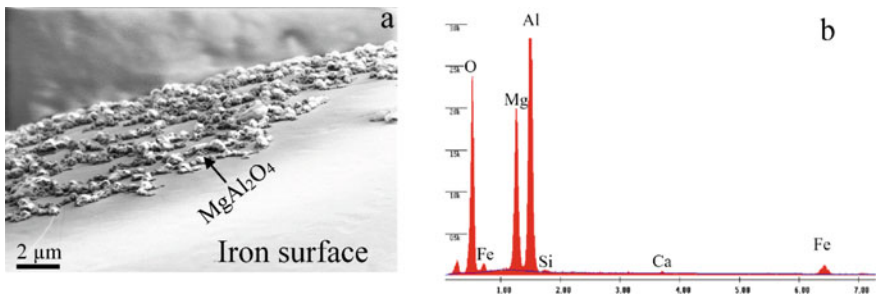**Fig. 21.10** Contact angle of Armco iron on the pure ceramic substrates [18]

Fig. 21.11 **a** Spinel formation on iron surface after contacting with MR 66 and **b** corresponding EDX analysis [18]

variation of contact angle was considered caused by the presence of TiO_2. Later, a newly formed phase with consistent of Ti, Si, and Mn in the cross section between AZT substrate and Armco iron was detected. Iron was found to infiltrate into the AZT substrate as well. On the contrary, no reaction was observed with the rested of the substrates, only a percent of SiO_2 was found to deposit on the surface of substrates. Furthermore, $MgAl_2O_4$ spinel on the surface of solidified iron after contacting with MR 66 substrate was determined, as presented in Fig. 21.11.

21.3.3 Inclusions

Figure 21.12 presents the inclusions number with various sizes after making contact with the various substrates. In comparison with the initial iron, the total number of
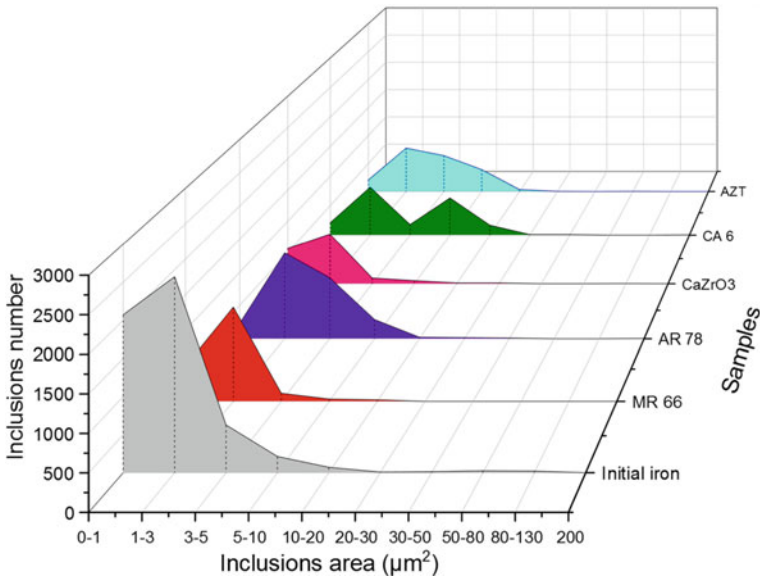
Fig. 21.12 Size distribution of inclusion particles per 100 mm^2 scanned area

inclusions decreased significantly after interaction experiments. The possible explanations for this phenomenon are predicted based on the experimental achieved results: (1). Transportation of inclusions on the sides of the substrates. Deposition of the SiO_2 inclusions at the interface of the pure substrates and into the AZT substrate were observed (2). Agglomeration of inclusions. In the initial Armco iron, the inclusions with the size of 1–3 μm^2 showed a peak (see Fig. 21.12 initial iron). However, after the interaction experiment, some peaks showed in the greater size ranges. The greater size of the inclusions indicates the agglomeration process in the liquid iron during the interaction. Three clusters formation mechanisms were proposed in previous investigations, i.e. 1. Collision of single inclusions into a cluster; 2. Single inclusion and cluster; and 3. Cluster to cluster. (3). Evaporation. The evaporation of some elements when the iron sample turns to the liquid state. Mn was found to accumulate on the interface of the solidified iron.

Calculation of the Stability of Oxides

The stability of the oxides MgO, Al_2O_3, $MgAl_2O_4$, $CaZrO_3$, ZrO_2, and CA 6 (the oxides formation reactions and the stability calculation method are listed in Table 21.4, free energy ΔG was calculated by utilizing FactSage 7.2 software (FactPS and FToxid), and activity for a_{Me}^x and $a_{Me_xO_y}$ are taken as unity). Figure 21.13 presents the calculated stability of the oxides, the measured oxygen partial pressures were marked in the diagram for the convenience of the comparison. In the pure substrates,

Table 21.4 Used reactions and equations for calculation of oxide stability [18]

$Mg + 2O_2 + 2Al = MgO \cdot Al_2O_3$	(21.9)	$K = \frac{a_{Me}^x P_{o2}^y}{a_{Me_X O_y}}$
$2Mg + O_2 = 2MgO$	(21.10)	
$2Al + 3/2O_2 = Al_2O_3$	(21.11)	$In(P_{o2}) = \frac{\Delta G}{RT}$
$2Ca + O_2 = 2CaO$	(21.12)	
$2Zr + O_2 = ZrO_2$	(21.13)	
$Ca + Zr + O_2 = CaZrO_3$	(21.14)	
$Ca + 19/2O_2 + 12Al = CaO \cdot 6Al_2O_3$	(21.15)	
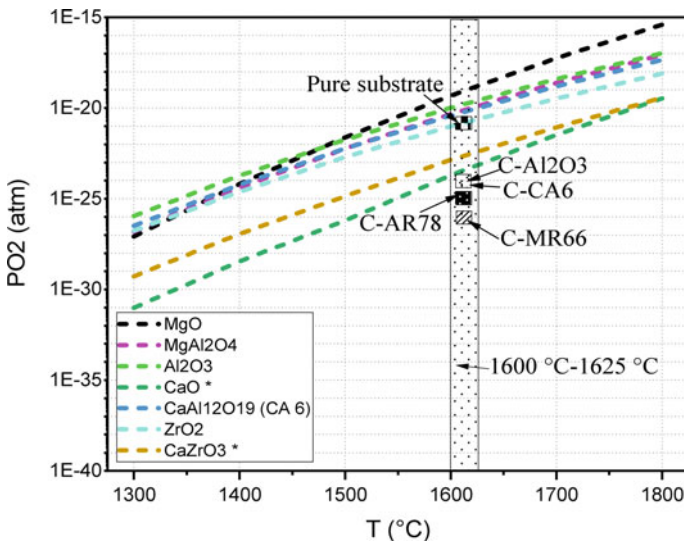
Fig. 21.13 The calculated stability of oxides as a function of temperature and the measured oxygen partial pressure at experimental temperatures

the measured oxygen partial pressure is around 10^{-22} atm at 1600 °C. With this oxygen partial pressure, oxides MgO, Al_2O_3, $MgAl_2O_4$, ZrO_2, and CA 6 could decompose. MgO oxide showed the lowest stability among these oxides. This explained the detected $MgAl_2O_4$ particles on the solidified iron droplet after contacting with MR 66 substrate, as shown in Fig. 21.11. On the other hand, it explains also why the oxygen partial pressure in the case of MR 66 is the lowest. It is due to the presence of the reoxidation of released metallic elements, Mg is easier to be released under the low oxygen partial pressure.

Oxygen partial pressures $P(O_2)$ up to 10^{-25} atm for C-AR 78 substrate, 10^{-26} atm for C-MR 66 substrate, and 10^{-24} atm for C-CA 6 and C-Al_2O_3 substrates and at temperature 1625 °C were measured. It is worth to mention that, the measured oxygen partial pressures were obtained at the gas outlet, i.e. the general oxygen partial pressures in the whole chamber were measured. In fact, the oxygen partial pressures in

spherical of carbon bonded substrates could be much lower than the measured values, it means that the decomposition of substrate would take place at low temperatures. It may explain why the iron samples were unshaped in the initial stage of melting process. According to the obtained experimental results and the calculated stability of various oxides, it can be concluded that instead of carbothermic reduction, these oxides would decompose at the present low oxygen partial pressure.

Influence on the Non-metallic Inclusions

The newly formed oxide layers on the iron samples were found to attract the non-metallic inclusions that existed in the iron sample. Inclusions such as SiO_2, CaO, and CaS were found attached to the newly formed oxide layer [20]. Moreover, the SiO_2 was detected as the core of a $MgAl_2O_4$ inclusion. It should be noted that in the initial iron sample SiO_2 was the main inclusion and its size was smaller than 3 μm^2 [18]. By working as a nucleation site, it significantly increased the size of the final inclusion, which is beneficial for the removing process since large inclusions can be easily filtered or removed by buoyancy force. A similar phenomenon was reported by Salomon et al. [7, 11].

On the other hand, the enrichment of metallic elements such as Mg, Al, and Ca in the liquid might result in a higher number of inclusions. However, during the filtration process of molten steel, the diffusion of metallic elements was firstly hindered by carbon at the filter's surface, then by the newly formed oxide layers. Besides this, the filtration time is short, usually in the range of 10–120 s [22]. Therefore, the carbon-bonded filters should not create impurities in the molten iron.

21.4   Conclusion

The present work was aim to analyze the interaction process between various oxides based filter materials with and without the addition of carbon. To complete this, the sessile drop method in a hot stage microscope under protective gas (Argon 5.0) was applied to ensure the cleanness of the experimental chamber. After the interaction experiments between pure substrates and liquid Armco iron, the ASPEX was applied to analyzed the inclusions in the solidified Armco iron including the size, amount, and the type of the inclusions. In general, after the interaction between liquid Armco iron and pure substrates, the most of the substrate remained non-corroded. However, a reaction layer was observed on the AZT substrate. Iron was found to infiltrate into the AZT substrate. Moreover, SiO_2 was found to deposit on the side of all substrates. The contact angle of the liquid Armco iron was also measured and presented. After the interaction experiments, the total number of the inclusions of the all cases decreased. Three factors were pointed out to explain the reduced inclusions number. (1). The increased size of some inclusions indicated the agglomeration of the inclusions;

(2). The transportation of the inclusions to the interface of the substrates; (3). The evaporation of some elements when the iron sample turns to the liquid state.

On the other hand, when carbon was added into the substrates, the interaction process was totally changed. The phenomena such as decarburization of carbon bonded substrates, the formation of whiskers, and oxide layers covered on the iron droplet was observed. In addition, the measured oxygen partial pressures changed with different substrates at the outlet of the hot stage microscope. In order to reveal the influence of iron, a piece of carbon bonded alumina was insert into a quartz glass ampule with an orifice and a platina container with lid and further heated in the hot stage microscope with the same period and temperature. The final results shown that the aluminum was released with the absence of iron. The detected results indicate the newly formed whiskers and oxide layer were caused only by the addition of carbon. Further, the stability of the substrates consisted oxides was calculated. The results showed that the most of the oxides could be decomposed under the low oxygen partial pressures. Moreover, the different oxygen partial pressures were caused also by the various stabilities of the oxides. In summary, with the presence of carbon, the released metallic elements were mainly caused by the low oxygen partial pressures and slightly dissolution.

References

1. J. Poirier, Metall. Res. Technol. **112**, 410 (2015). https://doi.org/10.1051/metal/2015028
2. A.L.V. da Costa e Silva, J. Mater. Res. Technol. **8**, 2408–2422 (2019). https://doi.org/10.1016/j.jmrt.2019.01.009
3. M. Emmel, C.G. Aneziris, Ceram. Int. **38**, 5165–5173 (2012). https://doi.org/10.1016/j.ceramint.2012.03.022
4. C.G. Aneziris, S. Dudczig, M. Emmel, H. Berek, G. Schmidt, J. Hubalkova, Adv. Eng. Mater. **15**, 46–59 (2013). https://doi.org/10.1002/adem.201200199
5. M. Emmel, C.G. Aneziris, F. Sponza, S. Dudczig, P. Colombo, Ceram. Int. **40**, 13507–13513 (2014). https://doi.org/10.1016/j.ceramint.2014.05.033
6. S. Dudczig, C.G. Aneziris, M. Emmel, G. Schmidt, J. Hubalkova, H. Berek, Ceram. Int. **40**, 16727–16742 (2014). https://doi.org/10.1016/j.ceramint.2014.08.038
7. A. Salomon, M. Dopita, M. Emmel, S. Dudczig, C.G. Aneziris, D. Rafaja, J. Eur. Ceram. Soc. **35**, 795–802 (2015). https://doi.org/10.1016/j.jeurceramsoc.2014.09.033
8. A. Schmidt, J. Fruhstorfer, S. Dudczig, C.G. Aneziris, Adv. Eng. Mater. **22**, 1900647 (2020). https://doi.org/10.1002/adem.201900647
9. T. Zienert, S. Dudczig, P. Malczyk, N. Brachhold, C.G. Aneziris, Adv. Eng. Mater. **22**, 1900811 (2020). https://doi.org/10.1002/adem.201900811
10. E. Storti, H. Berek, C.G. Aneziris, Ceram. Int. **44**, 14502–14509 (2018). https://doi.org/10.1016/j.ceramint.2018.05.065

11. A. Salomon, M. Motylenko, D. Rafaja, Adv. Eng. Mater. **24**, 2100690 (2022) https://doi.org/10.1002/adem.202100690
12. X. Wei, A. Yehorov, E. Storti, S. Dudczig, O. Fabrichnaya, C.G. Aneziris, O. Volkova, Adv. Eng. Mater. **24**, 2100718 (2022). https://doi.org/10.1002/adem.202100718
13. E. Storti, M. Farhani, C.G. Aneziris, C. Wöhrmeyer, C. Parr, Steel Res. Int. **88**, 1700247 (2017). https://doi.org/10.1002/srin.201700247
14. R. Khanna, S. Kongkarat, S. Seetharaman, V. Sahajwalla, ISIJ Int. **52**, 992–999 (2012). https://doi.org/10.2355/isijinternational.52.992
15. T. Zienert, S. Dudczig, O. Fabrichnaya, C.G. Aneziris, Ceram. Int. **41**, 2089–2098 (2015). https://doi.org/10.1016/j.ceramint.2014.10.004
16. C. Voigt, L. Ditscherlein, E. Werzner, T. Zienert, R. Nowak, U. Peuker, N. Sobczak, C.G. Aneziris, Mater. Des. **150**, 75–85 (2018). https://doi.org/10.1016/j.matdes.2018.04.026
17. T. Dubberstein, H.-P. Heller, J. Klostermann, R. Schwarze, J. Brillo, J. Mater. Sci. **50**, 7227–7237 (2015). https://doi.org/10.1007/s10853-015-9277-5
18. X. Wei, S. Dudczig, E. Storti, M. Ilatovskaia, R. Endo, C.G. Aneziris, O. Volkova, J. Eur. Ceram. Soc. **42**, 2535–2544 (2022). https://doi.org/10.1016/j.jeurceramsoc.2022.01.011
19. Z. Xie, F. Ye, J. Wuhan, Univ. Technol.Mater Sci Edn. **24**, 896–902 (2009). https://doi.org/10.1007/s11595-009-6896-1
20. X. Wei, E. Storti, S. Dudczig, A. Yehorov, O. Fabrichnaya, C.G. Aneziris, O. Volkova, J. Eur. Ceram. Soc. **42**, 4676–4685 (2022). https://doi.org/10.1016/j.jeurceramsoc.2022.04.058
21. J.J. Biernacki, G.P. Wotzak, J. Therm. Anal. **35**, 1651–1667 (1989). https://doi.org/10.1007/BF01912940
22. A. Schmidt, A. Salomon, S. Dudczig, H. Berek, D. Rafaja, C.G. Aneziris, Adv. Eng. Mater. **19**, 1700170 (2017). https://doi.org/10.1002/adem.201700170